Journal of Geophysical Research: Space Physics

RESEARCH ARTICLE
10.1029/2018JA025828

An Initial Study Into the Long-Term Influence of Solar Wind Dynamic Pressure on Jupiter's Thermosphere

J. N. Yates[1,2], L. C. Ray[3], and N. Achilleos[4,5]

[1]European Space Astronomy Centre, European Space Agency, Madrid, Spain, [2]Space and Atmospheric Physics, Imperial College London, London, UK, [3]Department of Physics, University of Lancaster, Lancaster, UK, [4]Department of Physics and Astronomy, University College London, London, UK, [5]Centre for Planetary Science, UCL-Birkbeck, London, UK

Key Points:
- Long-term solar wind variation leads to thermospheric heating
- Heating was not sufficient to explain Jupiter's high thermospheric temperatures
- Magnetosphere-ionosphere-thermosphere models need to be more physically realistic

Correspondence to:
J. N. Yates,
japheth.yates@esa.int

Citation:
Yates, J. N., Ray, L. C., & Achilleos, N. (2018). An initial study into the long-term influence of solar wind dynamic pressure on Jupiter's thermosphere. *Journal of Geophysical Research: Space Physics*, *123*, 9357–9369. https://doi.org/10.1029/2018JA025828

Received 27 JUN 2018
Accepted 3 OCT 2018
Accepted article online 11 OCT 2018
Published online 22 NOV 2018

Abstract Jupiter's thermosphere is ~700 K hotter than expected if it were heated only by solar extreme ultraviolet radiation. Other, more effective heat sources are therefore necessary to explain the high observed temperatures ≥900 K. It has been suggested that heating resulting from the atmospheric interaction with Jupiter's dynamic magnetosphere could account for the excess heat required. However to date, no numerical models have been successful at reproducing Jupiter's hot thermosphere without invoking essentially ad hoc heating mechanisms. Work presented in Yates et al. (2014, https://doi.org/10.1016/j.pss.2013.11.009) emphasized the importance of incorporating time dependence in magnetosphere-ionosphere-thermosphere coupling when simulating this aspect of the Jovian system. We extend their model (for a single magnetospheric compression or expansion) to simulate the response of thermospheric heating to multiple shocks and rarefactions in the solar wind for the first time. We employ a configurable magnetosphere model coupled to an azimuthally symmetric general circulation model. We compare the response of thermospheric temperatures to these consecutive magnetospheric reconfigurations over a period of 100 Jovian rotations. We find that the thermal structure of our model thermosphere does not respond significantly to such a prolonged period of magnetospheric reconfigurations. Thermospheric mean temperatures increase by a maximum of ~15 K throughout our simulation. The high-latitude and high-altitude thermosphere is most influenced by magnetospheric reconfigurations. While this simulation shows that magnetospheric reconfigurations can heat the thermosphere, it also shows the need to consider a more realistic representation of the coupled Jovian system as well as alternate sources of heating not dependent on the magnetosphere.

1. Introduction

The upper atmospheres of Jupiter and the other gas giants are much hotter than would be expected if they were heated solely by solar extreme ultraviolet (EUV) radiation. Jupiter's upper atmosphere is ~700 K hotter than theoretical modeling predicts (Seiff et al., 1998; Strobel & Smith, 1973; Yelle & Miller, 2004). This is known as the gas giant *energy crisis* and has eluded explanation for many decades. Many attempts have been made to explain Jupiter's high atmospheric temperatures, from breaking of gravity and acoustic waves (Hickey et al., 2000; Matcheva & Strobel, 1999; Schubert et al., 2003; Young et al., 1997) to auroral particle precipitation (Grodent et al., 2001; Waite et al., 1983), Joule heating (Millward et al., 2005; Smith et al., 2005; Waite et al., 1983), and ion drag (Miller et al., 2000; Millward et al., 2005; Smith et al., 2005). Atmospheric gravity waves are thought to have been observed by the Galileo probe during its descent into Jupiter's equatorial atmosphere. Work by Young et al. (1997) claims that the observed gravity waves are capable of accounting for Jupiter's high temperatures, but later studies by Matcheva and Strobel (1999) and Hickey et al. (2000) show that the observed waves not only heat the upper atmosphere but also cool it and the resultant net heating is too small to explain the high observed temperatures. Schubert et al. (2003) found that acoustic wave breaking could potentially account for Jupiter's high temperatures, but they are poorly constrained by observations at Jupiter.

Auroral particle precipitation, Joule heating, and ion drag result from the interaction between Jupiter's strong magnetosphere and its upper atmosphere, which consists of the neutral thermosphere and ionosphere. There has been much recent work on Jovian magnetosphere-ionosphere-thermosphere (MIT) coupling which represent the thermosphere with a general circulation model (GCM) and couple this to a magnetosphere-ionosphere (MI) model or simplified magnetospheric input (Achilleos et al., 1998, 2001;

Bougher et al., 2005; Majeed et al., 2009, 2016; Millward et al., 2005; Ray et al., 2015; Smith & Aylward, 2009; Tao et al., 2009, 2014; Yates et al., 2012, 2014).

Smith and Aylward (2009) coupled a simplified model of Jupiter's magnetosphere to a GCM of Jupiter's thermosphere. The model was capable of self-consistently including angular momentum transfer between the magnetosphere and thermosphere. Smith and Aylward (2009), similar to the study by Smith and Aylward (2008) for Saturn, found that meridional advection of momentum is the dominant mechanism by which angular momentum is transferred to the high-latitude thermosphere. Furthermore, the presence of the *ion drag fridge* effect means that heat from the magnetospheric interaction is trapped at high latitudes, while low latitudes remain cold (Smith et al., 2007). In order to reproduce the observed temperatures, Smith and Aylward (2009) included an additional component to Joule heating created by rapidly fluctuating low-latitude electric fields. Other coupled MIT models presenting steady state conditions are those of Tao et al. (2009), Bougher et al. (2005), and Majeed et al. (2009, 2016). The Tao et al. (2009) study used an axisymmetric coupled model similar to the Smith and Aylward (2009) model, but it includes a more realistic ionosphere and equatorial heating by acoustic waves based on the works of Schubert et al. (2003). The inclusion of these waves reproduces equatorial temperatures similar to those observed by the Galileo probe. The Bougher et al. (2005) and Majeed et al. (2009, 2016) models include a full three-dimensional GCM and are also able to reproduce the high observed thermospheric temperatures via Joule heating. The above models reproduce the observed temperatures by including ad hoc low-latitude heating, poorly constrained wave heating, or order-of-magnitude larger Pedersen conductances. While these may one day be constrained to high degrees, they are currently not supported by observational evidence and so the gas giant energy crisis remains unanswered.

Steady state solar wind variability was investigated by Yates et al. (2012) by adapting the Smith and Aylward (2009) model. They found that Joule heating and ion drag energy increased by ~190%; between compressed (45 R_J; one Jovian radius is 71,492 km) and expanded (85 R_J) configurations. The power used to accelerate magnetospheric plasma increased slightly from compressed to averaged (65 R_J) configurations and subsequently decreased for an expanded magnetosphere. Most recently, Ray et al. (2015) were the first to investigate the decoupling between thermospheric and magnetospheric flows by including field-aligned potentials (FAPs) in a MIT model by combining the works of Ray et al. (2010, 2012) with the Jovian GCM of Smith and Aylward (2009). Ray et al. (2015) found that self-consistently including FAPs into a coupled MIT model does not significantly influence the Jovian thermospheric structure and dynamics. Temperature variations between simulations with FAPs and previous simulations without FAPs show ~1–2% changes in temperatures in high-latitude regions with small changes in neutral flows. These authors show that changes in the Pedersen conductance between the simulations have a greater effect on the neutral dynamics than rotational decoupling between the ionosphere and magnetosphere.

Most gas giant MI/MIT coupling studies consider the system under equilibrium conditions when in reality planetary systems are constantly perturbed. At Jupiter, two important and time-dependent drivers of magnetospheric dynamics which effect the atmosphere are the solar wind and Io's volcanism. The amount of plasma in Jupiter's magnetosphere is dependent on the volcanic activity on Io (e.g., Yoshikawa et al., 2017) and is the focus of future studies. The dynamic pressure of the solar wind often has order-of-magnitude rapid variations which act to either compress or expand the Jovian magnetosphere. Yates et al. (2014) investigated the influence of order-of-magnitude rapid (≤3 hr) variations in solar wind dynamic pressure on Jupiter's thermosphere. Similar to Cowley & Bunce (2003a, 2003b), Cowley et al. (2007) and Yates et al. (2014) found that magnetospheric compressions cause the supercorotation of magnetospheric plasma which reverses the flow of currents, angular momentum, and energy between the atmosphere and magnetosphere. Expansions cause an increase in the degree of subcorotation of magnetospheric plasma but do not alter the steady state flow of energy and angular momentum (i.e., from atmosphere to magnetosphere). From a thermospheric perspective, rapid magnetospheric reconfigurations ($\pm 35 R_J$) lead to an increase in high-latitude neutral temperatures (25–50 K) partly due to Joule heating. Expansions result in a factor-of-five increase in the energy dissipated by Joule heating and ion drag in the model thermosphere and used to accelerate magnetospheric plasma. Compressions lead to an increase in Joule heating and a decrease in ion drag. Compressions also significantly increase equatorward winds capable of transporting heating from the magnetospheric interaction from higher to lower latitudes.

Another recent study focusing on the temporal variability of the Jovian thermosphere is Tao et al. (2014). Here Tao et al., investigated how Jupiter's thermosphere-ionosphere responded to variability in the solar EUV flux on both long and short time scales. Tao et al. (2014) found a positive correlation between long-term solar EUV flux and Jovian thermospheric temperatures and velocities. The authors propose that increases in solar EUV lead to increases in the degree of magnetospheric plasma corotation and field-aligned currents. For shorter-term (order 20 Jovian rotations) variability in solar EUV flux, Tao et al. (2014) find that temperatures and winds at midlatitudes increase as the EUV flux increases and then later due to the propagation of energy from auroral latitudes where Joule heating is enhanced.

There are few remote observations of gas giant upper atmospheres and even fewer are in situ measurements. MIT modelers use these observations to constrain and validate simulation outputs. The H_3^+ ion is the major constituent of the Jovian and Kronian ionospheres, and due to its relatively long lifetime and bright auroral infrared (IR) emission, it can act as a tracer of ionospheric dynamics and provide estimates for the temperature of the thermospheric neutrals (e.g., Drossart et al., 1993, 1989; Lam et al., 1997; Lystrup et al., 2008; Miller et al., 1990; Stallard et al., 2001, 2002). Ultraviolet and infrared emission from H_2 can also be used to determine ionospheric and neutral thermospheric temperatures (see Kita et al., 2018; Yelle et al., 1996, and references therein). Neutral temperatures determined from remote observations are of similar order to in situ Galileo probe measurements near Jupiter's equator (Seiff et al., 1998). Melin et al. (2006) analyzed an auroral heating event observed by Stallard et al. (2001, 2002) which resulted in an ionospheric temperature increase from 940 to 1065 K over 3 days (8–11 September 1998). They found that heating from auroral particle precipitation could not account for the increase in temperature but that a combined estimate of ion drag and Joule heating rates between the 3 days (67 to 277 mW/m^2) was sufficient to explain the observations. Cooling rates by hydrocarbons and H_3^+ emission were also found to increase during this event but to a much lesser extent (~20% of the determined heating rates) suggesting that the thermosphere would be unlikely to return to its initial temperature state before the arrival of a subsequent heating event. This led Melin et al. (2006) to postulate that such heating events could increase equatorward winds, transporting more thermal energy from the auroral regions to lower latitudes as proposed by Waite et al. (1983).

In this study, we use the Jovian Axisymmetric Simulator, with Magnetosphere, Ionosphere and Neutrals (JASMIN) model (Smith & Aylward, 2009; Yates et al., 2014) to present the first simulation investigating the influence of long-term solar wind variability on Jupiter's thermosphere. We employ almost the same model setup as in Yates et al. (2014) but now simulate the thermosphere's response to 100 magnetospheric reconfigurations determined from PIONEER 10/11 observations upstream of Jupiter. In section 2 we described the coupled model employed here and the changes compared to previous simulations. Our simulation results and discussion are presented in sections 3 and 4. We conclude in section 5.

2. Model Description

2.1. Coupled MIT model

The coupled numerical model employed for this study is based on the model described by Yates et al. (2014). As such, we give only a brief description here to describe the differences between the model employed here and that discussed in Yates et al. (2014).

The thermosphere model employed here remains unchanged from Yates et al. (2014). It is a GCM solving the Navier-Stokes equations of energy and momentum and the continuity equation using explicit time integration (Müller-Wodarg et al., 2006). The model solves the three-dimensional equations assuming azimuthal symmetry resulting in an essentially two-dimensional model in pressure and latitude coordinates. The latitudinal grid resolution is 0.2°, and the altitude/pressure resolution is 0.4 pressure scale height. The lower boundary is located at 0.2 μbar (300 km above the 1 bar (B) level) and its upper boundary is at 0.02 nbar. Our simplified ionosphere model is exactly the same as described in Yates et al. (2014) and consists of a vertical and latitudinal component. Vertical ionospheric density profiles are taken from Grodent et al. (2001)'s 1-D model and determine how our Pedersen and Hall conductivities vary with altitude. Latitudinal variations of height-integrated Pedersen conductance Σ_P are prescribed by the user in this study, and the vertical conductivity profile is scaled such that Σ_P calculated from the vertical profiles matches that prescribed by the user (Nichols & Cowley, 2004). In the auroral region (latitudes 60–74°) our model assumes a constant Σ_P of 0.5 mho. Poleward of the auroral region (latitudes >74°) $\Sigma_P = 0.2$ mho (Isbell et al., 1984) while for latitudes <60° $\Sigma_P = 0.0275$ mho (Hill, 1980).

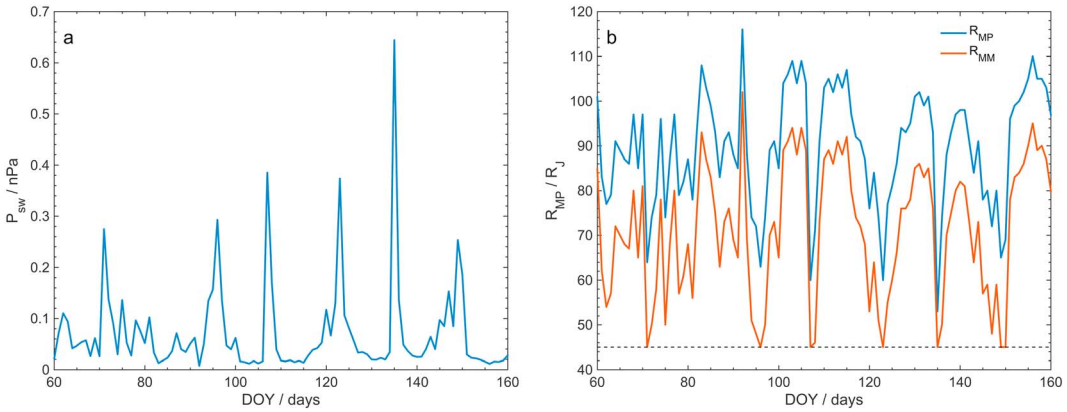

Figure 1. PIONEER 10/11 derived solar wind dynamic pressures (a) and the resulting magnetopause (R_{MP}) and magnetodisc (R_{MM}) radii (b) as a function of day of year (DOY) in 1974.

Our axisymmetric magnetosphere model is based on a combination of the models by Nichols and Cowley (2004) and Cowley et al. (2005, 2007) and is fully described in Yates et al. (2012, 2014). Other than the equatorial magnetic field strength $B_{ze}(\rho_e)$, we calculate the ionospheric flux function $F_i(\theta_i)$ and its magnetospheric equivalent $F_e(\rho_e)$. Surfaces of constant flux function represent magnetic shells with common ionospheric colatitudes θ_i and equatorial radial distances ρ_e. Therefore, by equating the ionospheric and magnetospheric flux functions, we can map radial distances in the magnetospheric equatorial plane to colatitudes in the ionosphere. In addition, by assuming that the total magnetic flux in the system is conserved, we can reconfigure the magnetosphere model to different sizes.

These models are coupled in such way that the atmospheric component solves the Navier-Stokes equations of motion and passes a thermospheric neutral angular velocity Ω_T profile (see Smith & Aylward, 2009, for details on exactly how this is calculated) to the magnetospheric component. The magnetospheric module solves a set of equations including the Hill-Pontius equation (Hill, 1979; Pontius, 1997) in order to determine the torque balance between the outward diffusion of iogenic plasma in the magnetosphere and the $\mathbf{J}\times\mathbf{B}$ force associated with MI currents (Yates et al., 2012). This results in a radial plasma angular velocity Ω_M profile for the magnetosphere. Having both thermospheric neutral and magnetospheric angular velocity profiles and height-integrated Pedersen conductances allows for the determination of the MI coupling currents which then feed back onto the thermosphere. Specifically, the intensity of these currents determines ionospheric current density and related ion drag force / Joule heating rate. For detailed information about how this model is coupled and the equations that are solved the reader is referred to Smith and Aylward (2009), Yates et al. (2012), and Ray et al. (2015).

2.2. Including Long-Term Solar Wind Dynamic Pressure Variability

We use Pioneer 10/11 observations upstream of Jupiter to calculate the solar wind dynamic pressure (Figure 1a) and use the model of Joy et al. (2002) to determine the corresponding subsolar magnetospheric size (Figure 1b). This gives us a time series of magnetospheric sizes which we use to drive our simulation. We begin our simulation with an initially expanded ($R_{MM} = 85\ R_J$) steady state model.

Each Jovian rotation can be split into two portions as shown in Figure 2: (i) a dynamic portion where the magnetosphere is reconfigured and (ii) a steady state portion where the magnetosphere is considered to be in or near equilibrium. For the steady state portion, plasma angular velocity profiles are obtained by solving the Hill-Pontius equation in the same manner as described in Smith and Aylward (2009) and Yates et al. (2012) but with a fixed height-integrated Pedersen conductance. During reconfigurations we employ the same assumption as Yates et al. (2014) where magnetospheric plasma angular momentum is conserved as long as these reconfigurations occur over small time scales ($\leq$ 3 hr; Cowley et al., 2007). Our approach differs from that of Yates et al. (2014) in that here the magnetosphere is reconfigured at the start of each rotation instead of the end in order to investigate the longer-term response of the thermosphere. The limitations of our approach are discussed in detail in section 4.2.

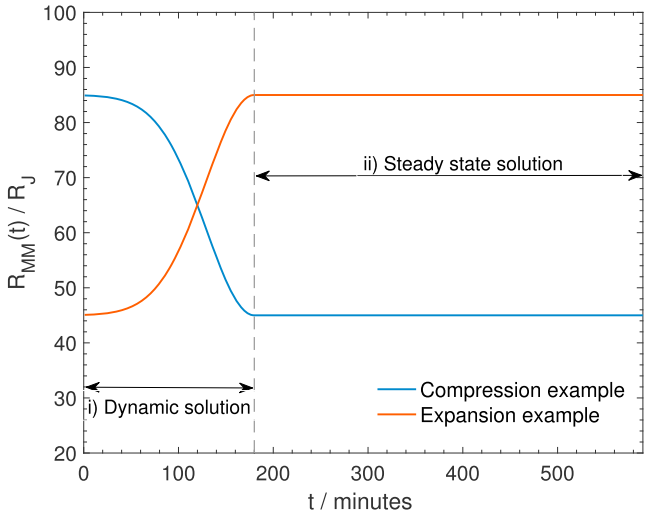

Figure 2. Magnetospheric reconfiguration example. The reconfiguration (compression or expansion) occurs during the first 180 min of a Jovian rotation where we solve for plasma angular velocity as in Yates et al. (2014). After the reconfiguration we switch to a steady state solver as in Yates et al. (2012).

3. Results

3.1. Initial Steady State of the Simulation

At the start of our simulation (simulation day 1 or DOY 60 in Figure 1), the magnetosphere is in an expanded state with a magnetodisc radius $R_{MM} = 85\ R_J$. The MI coupling currents and atmospheric dynamics for this steady state configuration have been discussed at length in Yates et al. (2012, 2014), and here we simply describe their general features. Figure 3 shows the east-west (a) and north-south (b) winds and the temperature (c) distribution of the neutral atmosphere as a function of pressure and latitude. The east-west (zonal) winds in Figure 3a show the much discussed high-latitude subcorotational jet (large negative velocities), and equatorward of this jet lies a low-altitude supercorotational jet. There is also a second, much weaker, subcorotational jet at high altitudes and midlatitudes. Figure 3b shows that there exist strong poleward winds (negative north-south velocities) at low altitudes and poleward of ~70°, while at higher altitudes there exist equatorward but weaker winds. Heating from the magnetospheric interaction (Joule heating and ion drag) is deposited at low altitudes where these strong poleward winds transport it toward the pole. At higher altitudes, the equatorward winds transport heat toward lower latitudes but this is not efficient as these high-altitude winds are weak. This results in equatorial and midlatitudes being generally very cold in comparison to polar latitudes and observations (Lam et al., 1997; Lystrup et al., 2008; Seiff et al., 1998). The high-latitude thermosphere in our simulation is colder than the observed temperatures.

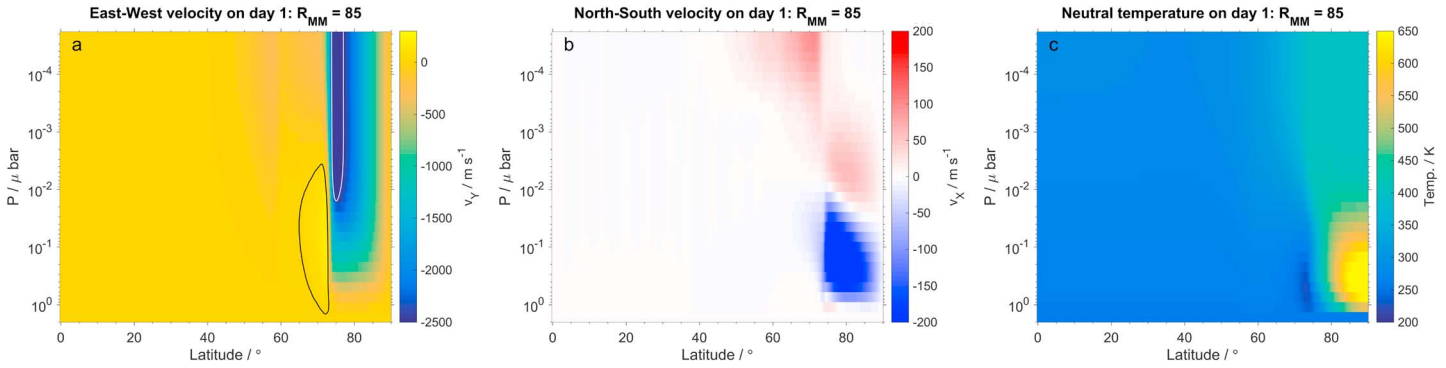

Figure 3. Pressure-latitude distributions of the east-west (a) and north-south (b) neutral winds and the neutral temperature (c) for the initial steady state of the simulation. Negative velocities are subcorotational (westward) for the east-west winds and poleward for the north-south winds. Positive velocities are therefore supercorotational and equatorward for the east-west and north-south winds, respectively. The black contour in (a) encloses regions of supercorotation greater than 25 m/s, while the white contour encloses regions of subcorotation slower than −2,500 m/s.

3.2. Simulation Snapshots

We now present three typical snapshots from our 100-day simulation: days 51 (DOY 111), 76 (DOY 136), and 100 (DOY 160). The left column of Figure 4 shows, from top to bottom, the east-west (a) and north-south (d) winds and the temperature (g) distribution of the neutral atmosphere as a function of pressure and latitude for simulation day 51. Figure 4j shows the corresponding temperature difference between days 51 and 1 (initial state). The middle and right columns of Figure 4 show the same but for days 76 and 100, respectively.

On simulation day 51, the neutral zonal wind (Figure 4a) structure does not change significantly. The high-latitude supercorotational and subcorotational jets both become slightly more corotational. The midlatitude subcorotational jet becomes more subcorotational, while three new supercorotation regions develop (see black contours showing velocities >25 m/s). In contrast, the recurring magnetospheric reconfigurations have drastically altered the north-south winds (see Figure 4d). The strong low-altitude, high-latitude poleward flows are still present, but now strong poleward flows are also present at high altitudes in the polar region. Equatorward of ~70°, there are alternating bands of strong equatorward and poleward flows. Figure 4g shows the temperature distribution of the thermosphere. The overall structure is not very different from that seen at the beginning of our simulation—cold equatorial latitudes and hot polar latitudes. However, looking at the difference between the temperature on days 51 and 1 (see Figure 4j), we can see that there are temperature variations between −10 and +80 K. The polar thermosphere is generally ~40 K warmer than in the initial state, and the equatorial region has vertical warm and cold (±10 K) temperature bands which coincide with the north-south wind structures. A primary source of heating at latitudes >60° comes from recurring changes in Joule heating and ion drag. However, on simulation day 51 there is also a significant contribution from adiabatic heating. This is particularly true for the high-altitude polar region where the temperature is ~80 K hotter than on day 1. Adiabatic heating and cooling are also responsible for the equatorial warm-cold vertical temperature bands where there are strong north-south and vertical (not shown) wind shears.

On simulation day 76, the magnetosphere is compressed significantly from a magnetodisc radius of 76 R_J to 45 R_J. Yates et al. (2014) showed that large and rapid compressions cause magnetospheric plasma to supercorotate compared to the planetary and thermospheric rotation rates. The magnetosphere essentially *spins-up* the thermosphere, and we see this in Figure 4b where the zonal winds throughout the thermosphere show a stronger degree of corotation. Figure 4e shows the north-south neutral winds. The low-altitude poleward winds are weaker than on day 1, and the high-altitude equatorward winds are now much stronger. Figures 4h and 4k show the neutral temperature and temperature difference distribution, respectively. There is a significant (order 100 K or ~10% of the peak temperature) decrease in neutral temperature at low altitudes in the polar region. This is likely caused by an ~70% reduction in Joule heating and ion drag in this region combined with the large reduction in north-south winds transporting this heat poleward. At higher altitudes Joule heating and ion drag energy essentially cancel each other out and the hot regions are heated by the horizontal advection of energy while the cold regions are created by adiabatic cooling.

The simulation ends on day 100 with an expanded magnetosphere that is 2 R_J larger than the simulation's initial state. The zonal winds in Figure 4c are very similar to those in Figure 3a. The north-south winds are also very similar to our initial state but with an equatorward extension of equatorward flow. We also see a few small polar poleward flow regions. The temperature of the high-latitude thermosphere is ~25 K warmer than our initial state, while low latitudes remain unchanged. These small temperature differences also coincide with the least drastic magnetospheric reconfiguration (+14 R_J for days 50–51, −31 R_J for days 76–75, and −3 R_J for days 100–99). This small reconfiguration and the similarity with the simulation's initial state suggest that the hotter high-latitude thermosphere on day 100 is likely due to previous, more drastic magnetospheric reconfigurations and that the thermosphere is closer to an equilibrium state compared to the earlier two snapshots.

3.3. Summary of Simulation Output

Figures 5a–5c show the minimum, mean, and maximum thermospheric temperature as a function of simulation days, respectively. Figure 5d shows how the magnetodisc radius varies with simulation time. The minimum and maximum temperatures are well correlated with the size of the magnetosphere, while the mean temperature has a more complex relation with magnetospheric size. Figure 5b suggests that significant (>10 R_J) magnetospheric reconfigurations occurring in rapid succession do indeed increase the mean thermospheric temperatures.

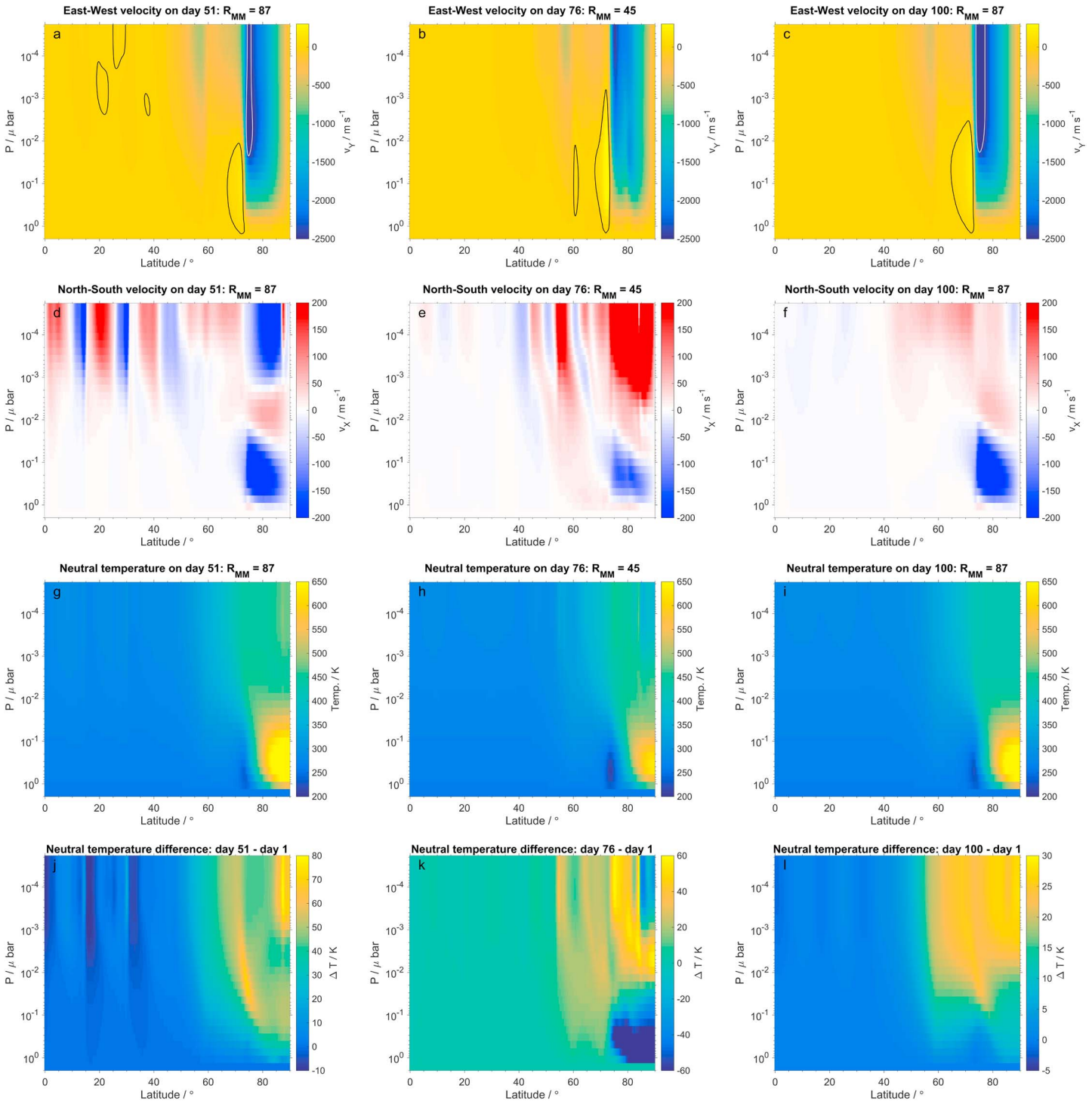

Figure 4. Pressure-latitude distributions of the east-west (a–c) and north-south (d–f) neutral winds and the neutral temperature (g–i) for 3 days in our transient simulation (days 51, 76, and 100 are shown in the left-, middle-, and right-hand columns, respectively). (j–l) Show the difference in temperature between days 51, 76, and 100 and the initial steady state (day 1). Negative velocities are subcorotational (westward) for the east-west winds and poleward for the north-south winds. Positive velocities are therefore supercorotational and equatorward for the east-west and north-south winds, respectively. The black contour in (a–c) encloses regions of supercorotation greater than 25 m/s, while the white contour encloses regions of subcorotation slower than −2,500 m/s.

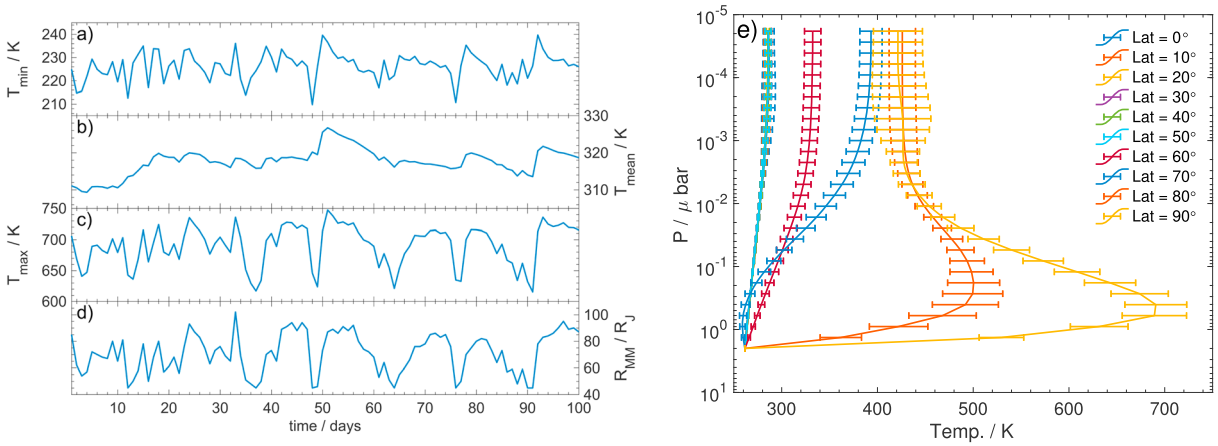

Figure 5. The minimum (a), mean (b), and maximum (c) temperature as a function of simulation time in days. (d) The magnetodisc radius R_{MM} as a function of simulation time. (e) The mean vertical neutral temperature profiles for latitudes between 0° and 90° in 10° steps. The error bars represent the standard deviation of the temperature profile at each vertical pressure level throughout the simulation time. Note that lines representing latitudes 0–50° lie on top of each other.

Figure 5e shows how the average vertical thermal structure of the thermosphere changes with latitude (colored lines; see figure legend) in our simulation. The error bars represent the temporal spread of thermospheric temperature at each pressure level. Figure 5e shows that magnetospheric reconfigurations

1. have essentially no effect on our model thermosphere for low altitudes and latitudes ≤50°,
2. do influence high-altitude temperatures at all latitudes but more so toward the pole, and
3. have the largest effect on latitudes ≥80°.

These summary plots imply that recurring magnetospheric reconfigurations do significantly influence the thermosphere, but this response is focused at high altitudes and latitudes.

4. Discussion

4.1. Energetics of the Magnetospheric Interaction

This study investigates the effect of recurring magnetospheric reconfigurations on Jupiter's upper atmosphere. As such we focus our discussion on heating related to the magnetospheric interaction. We realize that other heating and cooling terms play significant roles in planetary atmospheres, especially once perturbed, but detailed investigation of these other terms is saved for future studies.

The strength of the magnetospheric interaction with the atmosphere can be determined by looking at the power per unit area used to accelerate magnetospheric plasma toward corotation P_M as well as the power per unit area that is dissipated in the atmosphere via Joule heating P_{JH} and ion drag P_{ID} given by the following:

$$P = \Omega_J \tau, \qquad P_{\mathrm{JH}} = (\Omega_T - \Omega_M)\tau, \tag{1}$$

$$P_{\mathrm{ID}} = (\Omega_J - \Omega_T)\tau, \tag{2}$$

$$P_M = \Omega_M \tau, \tag{3}$$

where

$$\tau = \rho_i i_P B_i. \tag{4}$$

Here P is the total power per unit area of the ionosphere transferred from Jupiter's rotation, τ is the torque exerted by the $\mathbf{J}\times\mathbf{B}$ force per unit area of the ionosphere, and $B_i = 2\,B_J$ is the assumed magnitude of the radial ionospheric magnetic field in the polar region, $B_J = 426,400$ nT is the equatorial magnetic field strength on Jupiter's surface. We can then integrate these powers over latitude to obtain the magnetospheric, Joule heating and ion drag power per hemisphere. These are shown in Figure 6 as a function of magnetodisc radius. The solid blue dots represent integrated Joule heating (a), ion drag (b), and magnetospheric (c) powers for

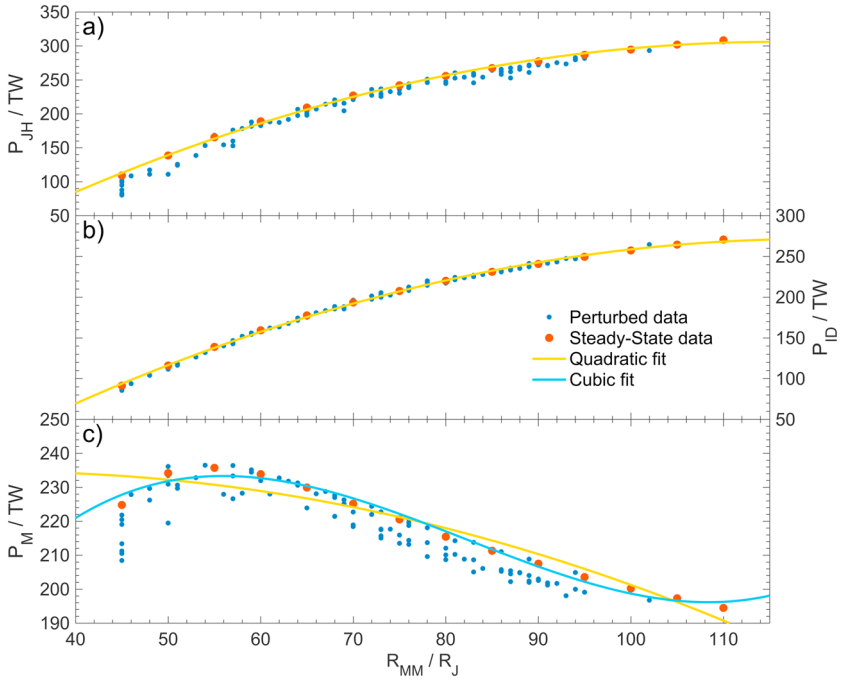

Figure 6. Integrated powers per hemisphere for Joule heating (a), ion drag (b), and magnetospheric power (c) as a function of magnetodisc size for the transient simulation are represented by the blue dots. Each blue dot represents powers at the end of each rotation in the simulation. The red dots show the same powers but for a steady state simulation with the same magnetospheric size. Each red dot represents one steady state simulation. Quadratic and cubic fits to these powers are represented by the yellow and cyan lines, respectively. Fit coefficients are given in Table 1.

each day in our simulation. The solid orange dots show the equivalent integrated powers in a steady state simulation with the same magnetodisc size. The yellow and cyan solid lines show quadratic and cubic fits to the steady state simulation output, respectively, and the fit coefficients are given in Table 1. One can immediately see from Figures 6a–6c that two trends emerge for both our perturbed 100-day simulation and the steady state simulations. The first is that Joule heating and ion drag integrated powers seem to increase with increasing magnetodisc size, and the second is that the magnetospheric power increases with magnetodisc size until $R_{MM} \sim 56\ R_J$ before decreasing. These general trends were also observed in the three steady state simulations of Yates et al. (2012).

We compare the integrated powers from this perturbed simulation with powers from steady state simulations of the same magnetospheric size and discuss the implications that recurring magnetospheric reconfigurations have on the gas giant energy crisis. To aid this comparison, we calculate the difference in integrated powers between the perturbed simulation and steady state fits, and we call these *residual* powers. These residuals are shown as a function of the change in magnetodisc radius in Figure 7.

In Figure 7 residual Joule heating, ion drag, and magnetospheric powers are represented by blue, red, and yellow dots, respectively. Figure 7 allows us to compare the difference in power between the perturbed and steady state simulations following magnetospheric compressions or expansions. It indicates that compres-

Table 1
Integrated Joule Heating, Ion Drag, and Magnetospheric Powers Fit Coefficients for the Steady State Simulations

Power	Fit type	p_0	p_1	p_2	p_3	R^2
Joule heating	Quadratic	-209.90 ± 24.30	8.90 ± 0.66	$(-38.41 \pm 4.20) \times 10^{-3}$		0.99
Ion drag	Quadratic	-181.70 ± 16.60	7.53 ± 0.45	$(-31.30 \pm 2.90) \times 10^{-3}$		0.99
Magnetospheric	Quadratic	227.20 ± 38.60	0.46 ± 1.04	$(-7.20 \pm 6.70) \times 10^{-3}$		0.93
	Cubic	16.31 ± 78.80	9.37 ± 3.27	-0.13 ± 0.04	$(0.52 \pm 0.19) \times 10^{-3}$	0.98

Note. Fits are polynomial of the form $p_0 + p_1\ R_{MM} + p_2\ R_{MM}^2 + p_3\ R_{MM}^3$.

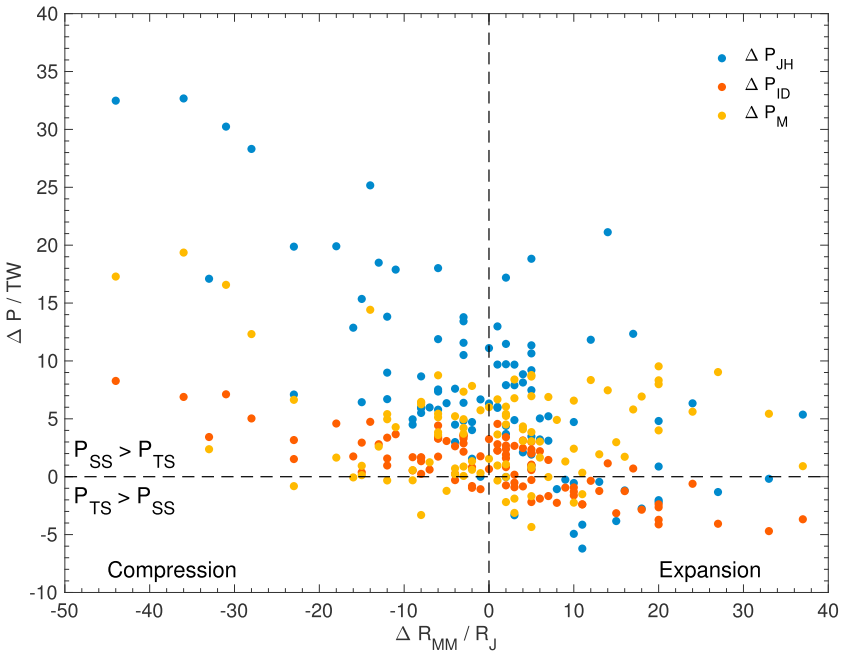

Figure 7. The residual integrated powers per hemisphere as a function of the change in magnetodisc size. Joule heating, ion drag, and magnetospheric powers are indicated by blue, red, and yellow dots, respectively. Positive (negative) residuals indicate that powers are greater (lower) in the steady state simulation compared to the time-dependent one. Positive (negative) ΔR_{MM} indicate magnetospheric expansions (compressions).

sive events, particularly, significant ones, lead to the largest difference between perturbed and steady state integrated powers with the latter being larger. Compressive events increase the degree of corotation of the plasma which causes a reversal in the flow of energy and angular momentum, spinning up the atmospheric neutrals and thus decreasing the shear between neutral, plasma, and the planetary (deep interior) angular velocities. As such we expect most compressive events to have lower integrated power resulting from the magnetospheric interaction than in an equivalently sized steady state system as is shown in Figure 7.

Expansion-type reconfigurations should therefore lead to the perturbed simulation having larger integrated powers than the steady state one, but this is not evident in Figure 7. Angular velocity profiles during expansive reconfigurations show that both the neutral and plasma profiles change less than for the compressive reconfigurations, and their profiles are not dissimilar to their steady state counterparts. This explains why the residual integrated powers are generally smaller and more evenly spread about zero compared to compressive reconfigurations. At first glance, angular velocity profiles during expansive reconfigurations do not behave as we would expect. However, the neutral thermosphere has significantly more mass and inertia than the magnetospheric plasma. When an expansive reconfiguration occurs and the magnetospheric plasma subcorotates to an even greater degree, this extracts energy and angular momentum from the neutrals, leading to a slight increase in subcorotation of the thermospheric neutrals. Once the reconfiguration ends and the coupled model relaxes back toward steady state, the neutrals are able to accelerate the magnetospheric plasma toward corotation and equilibrium. Figure 7 essentially suggests that the model thermosphere is closer to equilibrium for expansive magnetospheric reconfigurations than for compressive ones.

4.2. Limitations of the Current Model Setup

The model employed here is heavily based on that presented in Yates et al. (2014) and hence shares its limitations listed below.

1. Use of a fixed height-integrated Pedersen conductance in the auroral region (60–74° latitude). This does not significantly influence the thermosphere compared to using variable Pedersen conductance when considering a perfectly coupled MIT system, that is, no FAPs. For example, with regard to Joule heating and ion drag powers there are differences of a few percent between steady state simulations employing fixed (Yates et al., 2014) and variable (Yates et al., 2012) Pedersen conductances.

2. Assuming the thermosphere to be axially symmetric about the rotation axis. Smith and Aylward (2009) showed that this leads to modeling errors of ~20 % which is similar to, or less than, errors from other assumptions within the coupled model. Breaking the symmetry in the thermosphere and magnetosphere is the subject of ongoing work.
3. Using a fixed value for the plasma angular velocity mapping to latitudes >80° instead of one determined using solar wind dynamic pressure and the formulation of Isbell et al. (1984) was shown to be negligible for the range of magnetodisc sizes considered herein (Yates et al., 2014).
4. Not allowing for the development of FAPs and therefore rotational decoupling. Ray et al. (2015) found that inclusion of FAPs did not significantly alter the thermosphere compared to not including FAPs. However, they found that the changes in the Pedersen conductance due to FAPs had a larger effect on the thermosphere.

Our approach to simulate multiple magnetospheric reconfigurations is split into two portions as described in section 2.2. First, the dynamic portion where the reconfiguration occurs and second, the steady state portion where the model is assumed to be in its new equilibrium configuration. In the steady state portion we solve for the magnetospheric plasma flows using the Hill-Pontius equation and in the dynamic portion we assume that the plasma angular momentum is conserved as in Yates et al. (2014). The main caveat with this simulation is that we abruptly switch between the dynamic and steady state portions, meaning there is no *transition* phase between the dynamic and steady state portions where magnetospheric plasma flows are allowed to relax toward a new equilibrium. Ideally, we would like a single time-dependent and self-consistent way to solve for magnetospheric plasma angular velocity but this is beyond the scope of this study and the subject of future work. The impact of this abrupt change in regime is unlikely to significantly affect the neutral thermosphere considering that the Pedersen conductance is fixed, and we simply allow the thermosphere to respond to changes in magnetospheric plasma flows. Fortuitously, the inertia of the thermosphere benefits our simulation as it means that the magnetospheric plasma sees, and is influenced by, a perturbed neutral atmosphere with nonsteady state flows and so the new steady state plasma angular velocity solution will differ from a true steady state solution. Consequently, while not ideal, we believe that this perturbed simulation is able to shed light on the relatively long term response of Jupiter's upper atmosphere to multiple magnetospheric reconfigurations.

5. Conclusions

The interaction between Jupiter's upper atmosphere and its strong magnetosphere is a plausible candidate to explain Jupiter's high thermospheric temperatures (Yelle & Miller, 2004). This interaction leads to energy deposition in the auroral regions via particle precipitation, Joule heating, and ion drag. Energy from these sources is transported away from the auroral regions; however, in the current steady state GCMs the majority of this *magnetospheric heating* is transported to the poles by strong poleward winds. Equatorward winds are typically very weak and do not transport much heat toward the equator. We have used Pioneer 10/11 observations upstream of Jupiter to calculate solar wind dynamic pressures in order to investigate the long-term influence of solar wind on the upper atmosphere of a gas giant planet. The present study covers 100 reconfigurations, one per Jovian rotation. We then investigated Jupiter's thermospheric response to such a prolonged period of magnetospheric reconfigurations.

We find that north-south thermospheric winds are significantly influenced by these long-term reconfigurations, particularly at middle and low latitudes. The east-west winds are less affected by these reconfigurations and typically maintain a similar structure to the steady state. The overall thermal structure of our model thermosphere also remains relatively unchanged compared to previous work (Yates et al., 2014). Consecutive reconfigurations lead to slight increases in our predicted temperatures but when averaged over the entire thermosphere only amount to 7.60 K after 100 reconfigurations with a maximum of 15.70 K throughout the simulation. Maximum and minimum temperatures are found to be well correlated with magnetospheric size. High latitudes are also more influenced by magnetospheric reconfigurations than lower latitudes as the north-south winds which redistribute magnetospheric heating are generally too weak or, when they are strong, are not sustained for enough time to advect enough energy equatorward. Our work suggests that thermospheric heating due to solar wind forcing of the MIT coupled system cannot account for Jupiter's high thermospheric temperatures. This somewhat null result suggests that the magnetospheric interaction is unlikely to be solely responsible for the observed high temperatures of Jupiter's upper atmosphere. Therefore, other sources of heat, perhaps such as gravity and acoustic wave breaking, should also play crucial roles in

heating the Jovian thermosphere. It is worth noting that this conclusion is relevant for the axisymmetric coupled model presented herein. A full three-dimensional GCM coupled to a more realistic tilted magnetosphere model will lead to asymmetric (within and between each hemisphere) energy deposition from the magnetospheric interaction, potentially creating different thermospheric flows perhaps capable of more efficiently redistributing Joule heating and ion drag energy to lower latitudes.

Acknowledgments

J. N. Y. was supported by a European Space Agency research fellowship. L. C. R. acknowledges the STFC Consolidated Grant ST/R000816/1. N. A. was supported by the UK STFC Consolidated Grant (UCL/MSSL Solar and Planetary Physics, ST/N000722/1). The authors acknowledge the International Space Science Institute (ISSI) for their support of the *Coordinated Numerical Modeling of the Global Jovian and Saturnian Systems* team. J. N. Y. also thanks O. Witasse, N. Altobelli, S. Miller, T. Stallard, L. Moore, and P. Guio for useful discussions. The PIONEER 10/11 data sets used in this study are available from the Planetary Data System (http://pds.nasa.gov/) and are peer reviewed. Simulation output used in this study is available at https://doi.org/10.6084/m9.figshare.6707213.v1.

References

Achilleos, N., Miller, S., Prangé, R., Millward, G., & Dougherty, M. K. (2001). A dynamical model of Jupiter's auroral electrojet. *New Journal of Physics*, *3*, 3. https://doi.org/10.1088/1367-2630/3/1/303

Achilleos, N., Miller, S., Tennyson, J., Aylward, A. D., Mueller-Wodarg, I., & Rees, D. (1998). JIM: A time-dependent, three-dimensional model of Jupiter's thermosphere and ionosphere. *Journal of Geophysical Research*, *103*, 20,089–20,112. https://doi.org/10.1029/98JE00947

Bougher, S. W., Waite, J. H., Majeed, T., & Gladstone, G. R. (2005). Jupiter thermospheric general circulation model (JTGCM): Global structure and dynamics driven by auroral and Joule heating. *Journal of Geophysical Research*, *110*, E04008. https://doi.org/10.1029/2003JE002230

Cowley, S. W. H., Alexeev, I. I., Belenkaya, E. S., Bunce, E. J., Cottis, C. E., Kalegaev, V. V., et al. (2005). A simple axisymmetric model of magnetosphere-ionosphere coupling currents in Jupiter's polar ionosphere. *Journal of Geophysical Research*, *110*, A11209. https://doi.org/10.1029/2005JA011237

Cowley, S. W. H., & Bunce, E. J. (2003a). Modulation of Jovian middle magnetosphere currents and auroral precipitation by solar wind-induced compressions and expansions of the magnetosphere: Initial response and steady state. *Planetary and Space Science*, *51*, 31–56.

Cowley, S. W. H., & Bunce, E. J. (2003b). Modulation of Jupiter's main auroral oval emissions by solar wind induced expansions and compressions of the magnetosphere. *Planetary and Space Science*, *51*, 57–79. https://doi.org/10.1016/S0032-0633(02)00118-6

Cowley, S. W. H., Nichols, J. D., & Andrews, D. J. (2007). Modulation of Jupiter's plasma flow, polar currents, and auroral precipitation by solar wind-induced compressions and expansions of the magnetosphere: A simple theoretical model. *Annales de Geophysique*, *25*, 1433–1463.

Drossart, P., Bezard, B., Atreya, S. K., Bishop, J., Waite, J. H. Jr., & Boice, D. (1993). Thermal profiles in the auroral regions of Jupiter. *Journal of Geophysical Research*, *98*, 18,803–18,811. https://doi.org/10.1029/93JE01801

Drossart, P., Maillard, J.-P., Caldwell, J., Kim, S. J., Watson, J. K. G., Majewski, W. A., et al. (1989). Detection of H3(+) on Jupiter. *Nature*, *340*, 539–541. https://doi.org/10.1038/340539a0

Grodent, D., Waite, J. H., & Gérard, J. (2001). A self-consistent model of the Jovian auroral thermal structure. *Journal of Geophysical Research*, *106*, 12,933–12,952. https://doi.org/10.1029/2000JA900129

Hickey, M. P., Walterscheid, R. L., & Schubert, G. (2000). Gravity wave heating and cooling in Jupiter's thermosphere. *Icarus*, *148*, 266–281. https://doi.org/10.1006/icar.2000.6472

Hill, T. W. (1979). Inertial limit on corotation. *Journal of Geophysical Research*, *84*, 6554–6558. https://doi.org/10.1029/JA084iA11p06554

Hill, T. W. (1980). Corotation lag in Jupiter's magnetosphere—Comparison of observation and theory. *Science*, *207*, 301–302. https://doi.org/10.1126/science.207.4428.301

Isbell, J., Dessler, A. J., & Waite, J. H. Jr. (1984). Magnetospheric energization by interaction between planetary spin and the solar wind. *Journal of Geophysical Research*, *89*, 10,716–10,722. https://doi.org/10.1029/JA089iA12p10716

Joy, S. P., Kivelson, M. G., Walker, R. J., Khurana, K. K., Russell, C. T., & Ogino, T. (2002). Probabilistic models of the Jovian magnetopause and bow shock locations. *Journal of Geophysical Research*, *107*, 1309–1325. https://doi.org/10.1029/2001JA009146

Kita, H., Fujisawa, S., Tao, C., Kagitani, M., Sakanoi, T., & Kasaba, Y. (2018). Horizontal and vertical structures of Jovian infrared aurora: Observation using Subaru IRCS with adaptive optics. *Icarus*, *313*, 93–106. https://doi.org/10.1016/j.icarus.2018.05.002

Lam, H. A., Achilleos, N., Miller, S., Tennyson, J., Trafton, L. M., Geballe, T. R., & Ballester, G. E. (1997). A baseline spectroscopic study of the infrared auroras of Jupiter. *Icarus*, *127*, 379–393. https://doi.org/10.1006/icar.1997.5698

Lystrup, M. B., Miller, S., Dello Russo, N., Vervack, R. J. Jr., & Stallard, T. (2008). First vertical ion density profile in Jupiter's auroral atmosphere: Direct observations using the Keck II telescope. *Astrophysical Journal*, *677*, 790–797. https://doi.org/10.1086/529509

Majeed, T., Bougher, S. W., Ridley, A. J., Waite, J. H., Gladstone, G. R., & Bell, J. M. (2016). Global response of the upper thermospheric winds to large ion drifts in the Jovian ovals. *Journal of Geophysical Research: Space Physics*, *121*, 4647–4667. https://doi.org/10.1002/2015JA021328

Majeed, T., Waite, J. H., Bougher, S. W., & Gladstone, G. R. (2009). Processes of auroral thermal structure at Jupiter: Analysis of multispectral temperature observations with the Jupiter Thermosphere General Circulation Model. *Journal of Geophysical Research*, *114*, E07005. https://doi.org/10.1029/2008JE003194

Matcheva, K. I., & Strobel, D. F. (1999). Heating of Jupiter's thermosphere by dissipation of gravity waves due to molecular viscosity and heat conduction. *Icarus*, *140*, 328–340. https://doi.org/10.1006/icar.1999.6151

Melin, H., Miller, S., Stallard, T., Smith, C., & Grodent, D. (2006). Estimated energy balance in the Jovian upper atmosphere during an auroral heating event. *Icarus*, *181*, 256–265. https://doi.org/10.1016/j.icarus.2005.11.004

Miller, S., Achilleos, N., Ballester, G. E., Geballe, T. R., Joseph, R. D., Prangé, R., et al. (2000). The role of H_3^+ in planetary atmospheres, *Astronomy, physics and chemistry of H_3^+, royal society of London philosophical transactions series A* (Vol. 358, pp. 2485–2501). London, England: The Royal Society. https://doi.org/10.1098/rsta.2000.0662

Miller, S., Joseph, R. D., & Tennyson, J. (1990). Infrared emissions of H3(+) in the atmosphere of Jupiter in the 2.1 and 4.0 micron region. *The Astrophysical Journal Letters*, *360*, L55—L58. https://doi.org/10.1086/185811

Millward, G., Miller, S., Stallard, T., Achilleos, N., & Aylward, A. D. (2005). On the dynamics of the Jovian ionosphere and thermosphere. *Icarus*, *173*, 200–211. https://doi.org/10.1016/j.icarus.2004.07.027

Müller-Wodarg, I. C. F., Mendillo, M., Yelle, R. V., & Aylward, A. D. (2006). A global circulation model of Saturn's thermosphere. *Planetary and Space Science*, *180*, 147–160. https://doi.org/10.1016/j.icarus.2005.09.002

Nichols, J., & Cowley, S. (2004). Magnetosphere-ionosphere coupling currents in Jupiter's middle magnetosphere: Effect of precipitation-induced enhancement of the ionospheric Pedersen conductivity. *Annales de Geophysique*, *22*, 1799–1827.

Pontius, D. H. (1997). Radial mass transport and rotational dynamics. *Journal of Geophysical Research*, *102*, 7137–7150. https://doi.org/10.1029/97JA00289

Ray, L. C., Achilleos, N. A., & Yates, J. N. (2015). The effect of including field-aligned potentials in the coupling between Jupiter's thermosphere, ionosphere, and magnetosphere. *Journal of Geophysical Research: Space Physics*, *120*, 6987–7005. https://doi.org/10.1002/2015JA021319

Ray, L. C., Ergun, R. E., Delamere, P. A., & Bagenal, F. (2010). Magnetosphere-ionosphere coupling at Jupiter: Effect of field-aligned potentials on angular momentum transport. *Journal of Geophysical Research*, *115*, A09211. https://doi.org/10.1029/2010JA015423

Ray, L. C., Ergun, R. E., Delamere, P. A., & Bagenal, F. (2012). Magnetosphere-ionosphere coupling at Jupiter: A parameter space study. *Journal of Geophysical Research*, *117*, A01205. https://doi.org/10.1029/2011JA016899

Schubert, G., Hickey, M. P., & Walterscheid, R. L. (2003). Heating of Jupiter's thermosphere by the dissipation of upward propagating acoustic waves. *Icarus*, *163*, 398–413. https://doi.org/10.1016/S0019-1035(03)00078-2

Seiff, A., Kirk, D. B., Knight, T. C. D., Young, R. E., Mihalov, J. D., Young, L. A., et al. (1998). Thermal structure of Jupiter's atmosphere near the edge of a 5-μm hot spot in the north equatorial belt. *Journal of Geophysical Research*, *103*, 22,857–22,890. https://doi.org/10.1029/98JE01766

Smith, C. G. A., & Aylward, A. D. (2008). Coupled rotational dynamics of Saturn's thermosphere and magnetosphere: A thermospheric modelling study. *Annales de Geophysique*, *26*, 1007–1027.

Smith, C. G. A., & Aylward, A. D. (2009). Coupled rotational dynamics of Jupiter's thermosphere and magnetosphere. *Annales de Geophysique*, *27*, 199–230.

Smith, C. G. A., Aylward, A. D., Millward, G. H., Miller, S., & Moore, L. E. (2007). An unexpected cooling effect in Saturn's upper atmosphere. *Nature*, *445*, 399–401. https://doi.org/10.1038/nature05518

Smith, C. G. A., Miller, S., & Aylward, A. D. (2005). Magnetospheric energy inputs into the upper atmospheres of the giant planets. *Annales de Geophysique*, *23*, 1943–1947.

Stallard, T., Miller, S., Millward, G., & Joseph, R. D. (2001). On the dynamics of the Jovian ionosphere and thermosphere. I. The measurement of ion winds. *Icarus*, *154*, 475–491. https://doi.org/10.1006/icar.2001.6681

Stallard, T., Miller, S., Millward, G., & Joseph, R. D. (2002). On the dynamics of the Jovian ionosphere and thermosphere. II. The measurement of H_3^+ vibrational temperature, column density, and total emission. *Icarus*, *156*, 498–514. https://doi.org/10.1006/icar.2001.6793

Strobel, D. F., & Smith, G. R. (1973). On the temperature of the Jovian thermosphere. *Journal of Atmospheric Sciences*, *30*, 718–725. https://doi.org/10.1175/1520-0469(1973)030<0718:OTTOTJ>2.0.CO;2

Tao, C., Fujiwara, H., & Kasaba, Y. (2009). Neutral wind control of the Jovian magnetosphere-ionosphere current system. *Journal of Geophysical Research*, *114*, A08307. https://doi.org/10.1029/2008JA013966

Tao, C., Miyoshi, Y., Achilleos, N., & Kita, H. (2014). Response of the Jovian thermosphere to variations in solar EUV flux. *Journal of Geophysical Research: Space Physics*, *119*, 3664–3682. https://doi.org/10.1002/2013JA019411

Waite, J. H., Cravens, T. E., Kozyra, J., Nagy, A. F., Atreya, S. K., & Chen, R. H. (1983). Electron precipitation and related aeronomy of the Jovian thermosphere and ionosphere. *Journal of Geophysical Research*, *88*, 6143–6163. https://doi.org/10.1029/JA088iA08p06143

Yates, J. N., Achilleos, N., & Guio, P. (2012). Influence of upstream solar wind on thermospheric flows at Jupiter. *Planetary and Space Science*, *61*, 15–31. https://doi.org/10.1016/j.pss.2011.08.007

Yates, J. N., Achilleos, N., & Guio, P. (2014). Response of the Jovian thermosphere to a transient 'pulse' in solar wind pressure. *Planetary and Space Science*, *91*, 27–44. https://doi.org/10.1016/j.pss.2013.11.009

Yelle, R. V., & Miller, S. (2004). Jupiter's thermosphere and ionosphere, *Jupiter. The planet, satellites and magnetosphere* (pp. 185–218). Cambridge, UK: Cambridge University Press.

Yelle, R. V., Young, L. A., Vervack, R. J., Young, R., Pfister, L., & Sandel, B. R. (1996). Structure of Jupiter's upper atmosphere: Predictions for Galileo. *Journal of Geophysical Research*, *101*, 2149–2162. https://doi.org/10.1029/95JE03384

Yoshikawa, I., Suzuki, F., Hikida, R., Yoshioka, K., Murakami, G., Tsuchiya, F., et al. (2017). Volcanic activity on Io and its influence on the dynamics of the Jovian magnetosphere observed by EXCEED/Hisaki in 2015. *Earth, Planets, and Space*, *69*, 110. https://doi.org/10.1186/s40623-017-0700-9

Young, L. A., Yelle, R. V., Young, R., Seiff, A., & Kirk, D. B. (1997). Gravity waves in Jupiter's thermosphere. *Science*, *276*, 108–111. https://doi.org/10.1126/science.276.5309.108